ACS Catalysis

Research Article

pubs.acs.org/acscatalysis

A Class of (Pd−Ni−P) Electrocatalysts for the Ethanol Oxidation Reaction in Alkaline Media

Rongzhong Jiang,* Dat T. Tran, Joshua P. McClure, and Deryn Chu

Sensors and Electron Devices Directorate, U.S. Army Research Laboratory, 2800 Powder Mill Road, Adelphi, Maryland 20783-1197, United States

Supporting Information

ABSTRACT: A class of Pd−Ni−P electrocatalysts are prepared for the ethanol electrooxidation reaction (EOR). X-ray diffraction and transmission electron microscope reveal that the synthesized Pd−Ni−P catalyst possesses a more amorphous structure with smaller particle sizes when compared with a Pd−Ni sample without P and a control Pd black (Pd-blk) sample. The Pd−Ni−P catalyst contains double the number of electrocatalytically active sites (12.03%) compared with the Pd−Ni (6.04%) and Pd-blk (5.12%) samples. For the EOR, the Pd−Ni−P catalyst has the lowest onset potential (−0.88 V vs SCE), the most negative peak potential (−0.27 V vs SCE), and the highest EOR activity in 0.1 M KOH solution. Moreover, a 110 mV decrease in overpotential is observed for the EOR on the Pd−Ni−P catalyst compared with the Pd-blk catalyst. A Tafel slope of 60 mV/dec at low polarization potentials (<−0.76 V vs SCE) was obtained for EOR at a Pd−Ni−P-coated electrode with a reaction rate constant of 2.8×10^{-4} cm·S^{-1}·M^{-1} at −0.3 V vs SCE in KOH media. Finally, we find that the electrooxidation of ethanol on the Pd−Ni−P catalyst undergoes a 4-electron process to acetate.

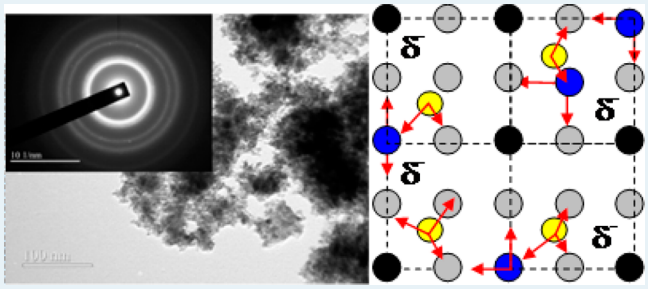

KEYWORDS: *Pd−Ni−P catalyst, ethanol electrooxidation, direct ethanol fuel cells, kinetics and mechanisms of EOR, substitutional/interstitial alloy*

1. INTRODUCTION

The membrane electrode assembly (MEA) for polymer membrane fuel cells consists of anode and cathode electrocatalysts separated by a polymer-electrolyte membrane. However, for proton-exchange membrane fuel cells (PEMFCs), the electrocatalysts account for ∼60% of the costs for fuel cell stacks,[1] which is primarily due to the use of platinum or platinum alloys. Moreover, the use of perfluorinated materials contributes to the high MEA costs. Prior investigations suggest that it may be possible to reduce the loading amount of noble metals such as platinum by making Pt core−shells,[2−4] alloying Pt with other transition metals,[2−4] or using high-surface-area carbon supports for better electrocatalyst utilization.[5−7] An alternative approach is to use non-Pt catalysts,[8,9] or non-noble metal catalysts[10−12] that replace traditional Pt-based catalysts. Unfortunately, neither non-Pt nor non-noble metal catalysts are stable in the presence of an acidic media under relevant fuel cell operating environments; therefore, alternative technologies must be pursued to drive down the fuel cell costs.

Alkaline electrolyte membrane (AEM) fuel cells have received much attention[13] because the high pH operating environment makes it possible to use non-Pt and non-noble metal electrocatalysts. For example, palladium (Pd) and Pd-based alloys are a type of non-Pt electrocatalysts, and although Pd is a noble metal, its cost is much lower because of its larger earth abundance. Many reports have shown that Pd-based alloys are candidates for catalytic alcohol and formic acid oxidation reactions.[14−21] In addition, more reports have been published, with an attempt to modify the electrocatalytic properties of noble metals of Pd and Pt by alloying them with other transition metals to create binary, ternary or quaternary metal/metal alloys, as well as incorporate a broad range of dopants. For example, nonmetals phosphorus (P) and boron (B) were used as dopants into noble metals, including Pd−P,[22,23] Pd−B,[24] Pd−Ni−P,[25] Pt−Ni−P,[26] Pt−Sn−P,[27] and Pd−Ni−Cu-P.[28] These nonmetal doped Pd and Pt electrocatalysts are different from the previously studied electrocatalysts in composition, electronic structure, and electrochemical performance. The various binary, ternary, and quaternary Pd and Pt electrocatalysts are essentially a class of electrocatalysts that may be able to electrocatalytically oxidize ethanol. Ethanol is an eco-friendly fuel, possesses a high theoretical energy density of 8030 Wh/kg, and is easily contained for transportation and delivery. Moreover, ethanol is also the second most extensively studied alcohol other than methanol for both acidic and alkaline electrolytes.[29−38] However, the ethanol molecule contains a carbon−carbon (C−C) bond that makes the complete oxidation a challenge. The payoff for being able to break the

Received: April 7, 2014
Revised: May 22, 2014
Published: June 23, 2014

   dx.doi.org/10.1021/cs500462z | ACS Catal. 2014, 4, 2577−2586

C−C bond for direct ethanol fuel cell would have a profound impact on the fuel cell area. This article focuses on synthesis, characterization, and the electrochemical performance of a ternary Pd−Ni−P electrocatalyst for the ethanol oxidation reaction (EOR) in alkaline media.

2. EXPERIMENTAL SECTION

2.1. Synthesis of Pd−Ni and Pd−Ni−P Catalysts. All chemicals were purchased from Sigma-Aldrich Chemical Company and were used as received. Pd−Ni alloy nanoparticles were synthesized using an in-house-developed wet chemical method. In a typical synthesis, 1.0 g of palladium chloride ($PdCl_2$), 5 mL of hydrochloride acid (HCl), and 100 mL of water were added into a 500 mL flask and stirred until fully dissolved. Next, another 100 mL of water and 0.68 g of nickel chloride hexahydrate ($NiCl_2{\cdot}6H_2O$) were added in the flask while stirring. At this point, the starting solution pH was 2.10. The reducing agent, 5 mL hydrazine monohydrate, was slowly dropped into the reactor, which resulted in a solution color change. The color during the reaction gradually changed as a result of the production of nanosized Pd−Ni alloy. The final pH of the reaction solution increased to 8.5 due to the excess reducing reagent. The precipitate was separated from the liquid via centrifugation and washed with water and alcohol repeatedly up to five times. After drying at ∼40−50 °C under vacuum overnight, ∼0.7 g of product was obtained. The Pd−Ni−P samples were synthesized in a manner similar to the aforementioned procedure for the Pd−Ni synthesis, except 0.6 g of sodium hypophosphite hydrate ($NaH_2PO_2{\cdot}xH_2O$) was added to the reaction solution prior to the addition of hydrazine monohydrate. The final Pd−Ni−P dry product obtained was ∼0.6−0.7 g. All synthetic experiments were carried out at room temperature (20 ± 1 °C).

2.2. Physical Characterizations of the Prepared Electrocatalysts. Transmission electron microscope (TEM) images were obtained with a high-resolution JEOL 2100 FE TEM equipped with an EDAX X-ray detector. Before imaging, a solution was prepared by adding 5 mg of the catalyst into 5 mL of 1-propanol, followed by a short ultrasonic bath (Branson 3510) treatment. An aliquot of ink was loaded onto the CF400-Cu Carbon film (Electron Microscopy Science) with a micropipette, and the sample was dried overnight at room temperature. Selected area electron diffraction (SAED) patterns and energy-dispersive X-ray spectroscopy (EDS) analysis were also obtained during the TEM measurements.

X-ray Diffraction Analysis (XRD) results were obtained from a Rigaku Ultima III instrument with Cu Kα radiation (λ = 1.5418 Å) using a Bragg−Brentano configuration. The measurements were conducted at a scan rate of 1.0° (2θ)/min, and each diffraction data point was collected at the interval of 0.02° (2θ) for the total spectrum range of 35−90° (2θ).

The Brunauer, Emmett, and Teller (BET) surface areas of the catalyst samples were measured with a Micromeritics TriStar II (TriStar II 3020 V1.03) using N_2 gas as the adsorbate at 77.3 K. Adsorption/desorption isotherm measurements were collected in the relative pressure range P/P_0 from 0.05 to 1.0. The samples were pretreated in an oven at 80 °C for 2 h and then degassed at 110 °C prior to the adsorption analysis.

2.3. Electrochemical Characterization of the Electrocatalysts. A Pine Bipotentiostat RDE4 was used for electrochemically analyzing the synthesized catalysts by depositing catalyst samples from ink mixtures onto a glassy carbon (GC) disk electrode. The catalyst ink contained 4 mg of total sample (Pd black, or Pd−Ni alloy, or Pd−Ni−P metal/nonmetal compound) per milliliter of solution (1:1 water/1-propanol + 5% Nafion solution). The ink was ultrasonically treated with a Branson Sonifier 450 at a duty 30 and output 8 for 10 min. Next, 10 μL of catalyst ink was coated onto a GC disk working electrode (0.196 cm^2) and dried at 30 °C under vacuum for ∼30−40 min. The final coating on the GC disk electrode contained 95% total catalyst and 5% Nafion with an electrocatalyst loading of 0.2 mg/cm^2. The catalyst-coated electrodes were mounted onto a Pine ASR rotator with the dried catalyst-coated GC disk electrodes used as the working electrode. All voltammetry experiments were performed in Ar-saturated KOH solution at room temperature (20 ± 1 °C) with and without adding ethanol. A platinum wire counter electrode and a saturated calomel reference electrode (SCE) were used for all studies. The current density reported in this article is based on the geometrical area of the GC disk electrode (mA cm^{-2}), which can be changed to (mA mg^{-1}) by simply multiplying a factor of 5 according to the mass of the catalyst loading.

2.4. Directly Doping of Phosphorus into Pd−Ni Catalyst Coated Electrode. A chemical solution for phosphorus doping was prepared by dissolution of 1.0 g of hypophosphite hydrate in 20 mL of water, and the pH was adjusted to 3.2 by adding a few drops of 0.5 M H_2SO_4. The Pd−Ni catalyst-coated GC electrode was soaked in the solution. The doping process was carried out in a vacuum chamber. The following reactions occurred in the thin layer of the Pd−Ni coating in the doping time:

$$H_2PO_2^- + H_2O \rightarrow H_2PO_3^- + H_2 \quad \text{(a)}$$

$$H_2PO_2^- + \frac{1}{2}H_2 \rightarrow P + H_2O \quad \text{(b)}$$

After 60 min of doping, the electrode was washed with water. The existence of phosphorus in the coating of Pd−Ni was determined using a method of cyclic voltammetry (CV) in 0.1 M KOH. The CVs of the same Pd−Ni catalyst electrode before and after doping phosphorus are compared to identify the phosphorus wave at the CVs, which is a specific signal of the existence of phosphorus in the catalyst coating.

In addition, an ink containing 47.5% red phosphorus (P), 47.5% carbon black (XC72R) and 5% Nafion was prepared with the assistance of ultrasound. This phosphorus-XC72R-coated GC electrode was examined with cyclic voltammetry for identifying the electrochemical oxidation of free state of phosphorus.

3. RESULTS AND DISCUSSION

3.1. Crystal Structure and Charge Transfer Relevance. It is well-known that the crystal structure of pure palladium metal belongs to the face centered cubic (fcc) family, which has lattice points on the faces of the cube. Each lattice point gives exactly one-half contribution, in addition to the corner lattice points, thus giving a total of 4 lattice points per unit cell (1/8 × 8 from the corners plus 1/2 × 6 from the faces). To understand the relevance among crystal structure and catalytic activity of palladium, Pd−Ni alloys, and the Pd−Ni−P compounds, we performed a qualitative analysis of the electronic charge transfer for each crystal.

Figure 1 shows the atom arrangement and electronic charge transfer analysis for four adjacent unit cells of the relevant fcc crystal structures. The black and gray spheres represent the Pd

dx.doi.org/10.1021/cs500462z | ACS Catal. 2014, 4, 2577−2586

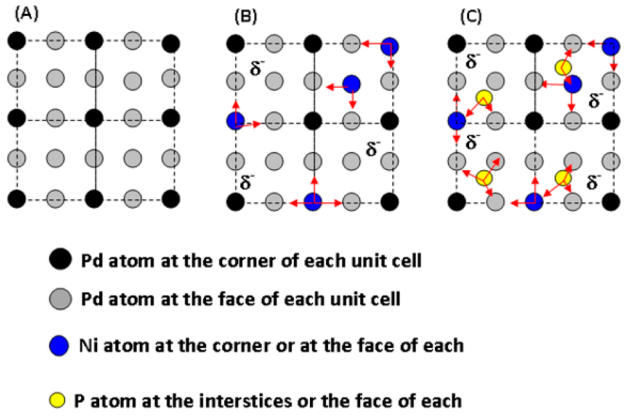

Figure 1. Atom arrangement and electronic charge transfer for 4 adjacent unit cells of face centered cubic crystal structures: (A) pure Pd crystal, (B) alloy Pd–Ni crystal, and (C) alloy Pd crystal doped with phosphorus (P) atoms.

atoms located in the corners and on the face, respectively, of the unit cells in Figure 1A. When lattice points occupied by the Pd atoms are replaced by Ni atoms, a substitutional alloy is formed because Pd and Ni have similar crystal structures (fcc) and atomic sizes. The Pd atoms become negatively charged in the Pd–Ni alloy because the ionization energy of Pd is higher than that of Ni,[19] which results in electronic charge transfer from the Ni atoms to the Pd atoms. The arrows in Figure 1B mark the electronic charge transfer directions, and the symbol "δ^-" denotes the negative charge state of the atoms.

Phosphorus is able to form an interstitial alloy with Pd or Ni metals becaue it is part of the triclinic crystal system, with a small atomic size. In the Pd–Ni–P compound, P atoms enter the interstitial spaces and form a mix of substitutional and interstitial alloying. The charge transfer between the P atoms and Ni atoms is dependent on the content of phosphorus.[39,40] For a low P content condition (i.e., < 25%), the charge transfer is directed from P atoms to Ni atoms.[39,40] Therefore, the Pd atoms in the Pd–Ni–P compound are further negatively charged by both Ni atoms and P atoms, which are illustrated in Figure 1C. As expected, the negatively charged Pd is more effective for the catalytic ethanol oxidation reaction because it facilitates the removal of intermediate products,[25,39] such as $(CH_3COO^-)_{ads}$ and $(CO)_{ads}$, and simultaneously prohibits the buildup of $(CO)_{ads}$ on the catalyst surface. The removal of the intermediate species and simultaneous mitigation of the buildup may lead to the desirable complete oxidation of ethanol (i.e., breakage of the C–C bond).[19]

3.2. Electrocatalyst Composition, Morphology and Structure. The Pd–Ni–P and Pd–Ni catalysts were analyzed with EDS, TEM, SAED, and BET. Supporting Information (SI) Figure S1 shows EDS patterns and corresponding elemental maps of Pd–Ni–P and Pd–Ni samples. The elemental maps show that Pd, Ni and P are dispersed uniformly for both the Pd–Ni–P and the Pd–Ni samples. From the EDS pattern, the relative compositions of the Pd–Ni–P and Pd–Ni samples yield the following compositions: $Pd_{0.8}Ni_{0.1}P_{0.1}$ and $Pd_{0.7}Ni_{0.3}$, respectively. Figure 2 shows TEM images of the Pd–Ni–P and Pd–Ni samples with approximately uniform particle size distributions. The Pd–Ni–P catalyst has slightly smaller particle sizes (~4–6 nm) compared with particle sizes measured for the Pd–Ni sample (~6–8 nm). The particle size of the Pd–Ni–P in this study is similar to a previous report by Y. Wang et al.,[25] who supported Pd–Ni–P on carbon black

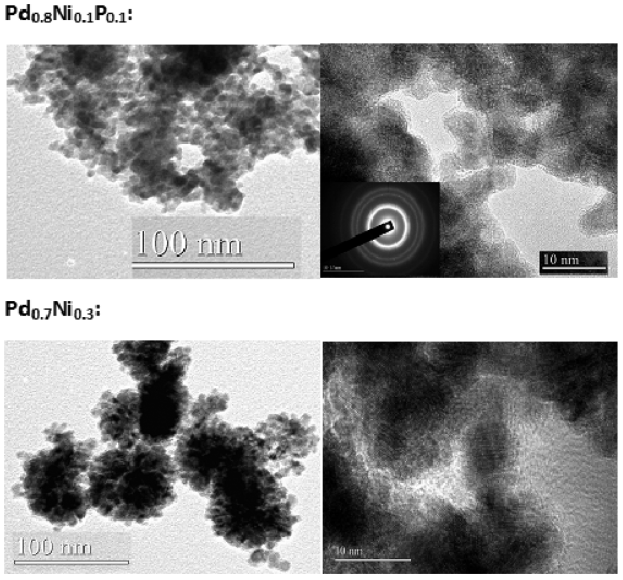

Figure 2. TEM image of catalyst samples $Pd_{0.8}Ni_{0.1}P_{0.1}$ and $Pd_{0.7}Ni_{0.3}$. The inset is a SAED pattern of the $Pd_{0.8}Ni_{0.1}P_{0.1}$ sample.

and found Pd–Ni–P particle sizes of 2–8 nm. In addition, the particle size of the Pd–Ni catalyst in this study matches well with the literature reported value of 5–10 nm.[15] A slightly smaller particle size was reported by Y. W. Gao et al.[14] for a Pd–Ni catalyst supported on carbon black with ~2–5 nm sizes. The TEM analysis is compared with the BET surface area of the catalysts in Table S1 (see SI). The surface area increases in the following order for Pd < Pd–Ni < Pd–Ni–P; however, the particle size decreases at the opposite trend as Pd–Ni > Pd–Ni–P. The inset in Figure 2 shows a SAED pattern for the Pd–Ni–P sample, which provided information on the perpendicular distance between adjacent lattice planes (i.e., the *d*-spacing). The information obtained from the SAED analysis is summarized in Table S2 (see SI). The *d*-spacings determined from the SAED pattern are consistent with the *d*-spacings obtained from XRD analysis.

Figure 3 shows the XRD patterns for Pd–Ni–P, Pd–Ni, Pd-black (Pd-blk), and Ni-powder samples. The peak for the (111) plane broadens when Ni and P are added to Pd. The broadening increase is in the following order: Pd < Pd–Ni < Pd–Ni–P. The broadening suggests that the resulting catalytic

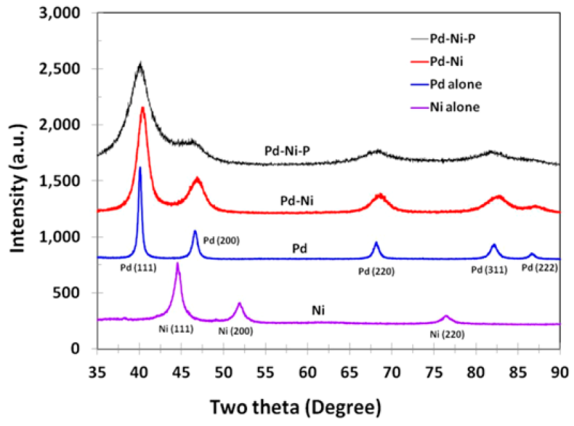

Figure 3. X-ray diffraction (XRD) patterns for $Pd_{0.8}Ni_{0.1}P_{0.1}$, $Pd_{0.7}Ni_{0.3}$, Pd, and Ni samples.

dx.doi.org/10.1021/cs500462z | ACS Catal. 2014, 4, 2577–2586

Table 1. Peak Position (2θ) and *d*-Spacing Collected from XRD Data

materials	plane (111)	plane (200)	plane (220)	plane (311)	plane (222)
Pd	40.04 (0.2246 Nm)	46.60 (0.1948 Nm)	68.04 (0.1376 Nm)	82.12 (0.1172 Nm)	86.30
$Pd_{0.7}Ni_{0.3}$	40.36 (0.2230 Nm)	46.74 (0.1936 Nm)	68.60 (0.1336 Nm)	82.50 (0.1165 Nm)	87.14
$Pd_{0.8}Ni_{0.1}P_{0.1}$	40.12 (0.2246 Nm)	46.22 (0.1945 Nm)	68.14 (0.1372 Nm)	81.84 (0.1176 Nm)	N/A

material develops a more amorphous structure after alloying with Ni or doping with phosphorus. Comparing the XRD patterns of the Pd−Ni−P and Pd−Ni samples with that of pure Ni, we have noticed three peaks at 2θ of ∼44.5°, ∼51.9°, and ∼76.5° for pure Ni, which are not seen for the Pd−Ni−P and Pd−Ni diffractograms. The disappearance of the Ni peaks for the Pd−Ni−P and Pd−Ni diffractograms demonstrates that the alloying process is complete, and no unalloyed nickel metal exists. Y. Wang et al.[25] reported the XRD results for carbon-supported PdNi/C and PdNiP/C and observed $Ni(OH)_2$ signals present for their PdNi/C sample. The presence of $Ni(OH)_2$ is different from our results, and the appearance for their PdNi/C catalyst is potentially due to a more facile oxidation of their catalyst's Ni nanoparticles attached on high-surface-area carbon. Table 1 lists the *d*-spacing and peak positions obtained from the XRD data of Pd−Ni−P, Pd−Ni, and Pd catalysts. As the peak shifts to larger 2θ values, the *d*-spacing decreases in the following order for the planes: (111) > (200) > (220) > (311). For the Pd−Ni sample, the 2θ peak position for plane (111) is larger, with a smaller *d*-spacing compared with the Pd sample, which implies that the Pd lattice structure shrinks after alloying with Ni. However, from the Pd−Ni to Pd−Ni−P samples, the 2θ value decreases, and the *d*-spacing increases, which indicates that the Pd−Ni lattice structure expands after doping with P atoms. In what follows, the variations in structure, composition, and morphology of each of the catalysts studied are correlated to the electrochemical performance for the catalytic ethanol electrooxidation.

3.3. Surface Electrochemistry of Catalyst-Coated Electrodes. The surface waves of the catalyst-coated electrodes were obtained in blank electrolyte solutions in the absence of ethanol and oxygen. Figure 4A shows cyclic voltammograms (CVs) for the Pd−Ni−P-, Pd−Ni-, or Pd-black-coated glassy carbon electrodes in argon-saturated 0.1 M KOH. For the Pd-black-coated electrode, a pair of symmetrical peaks is observed between −1.0 and −0.82 V and is assigned to the formation/desorption of proton−palladium species ($Pd-H_{ads}$):

$$Pd + H_2O + e^- \leftrightarrow (Pd - H_{ads}) + OH^- \quad (1)$$

The $Pd-H_{ads}$ formation/desorption peaks are smaller for the Pd−Ni or Pd−Ni−P electrodes compared with the Pd-coated electrode. After anodic scanning from −0.4 V to a more positive potential of +0.4 V, the anodic currents are relatively small and featureless for the Pd-blk-, Pd−Ni-, and Pd−Ni−P-coated electrodes because oxides are built up at the electrodes. During the anodic scanning, OH^- ions are adsorbed onto Pd to form a $Pd-OH_{ads}$ species (eq 2). At higher electrode potentials, the oxygen species are transferred to higher valence oxides, according to (eq 3):[41]

$$Pd + OH^- \rightarrow (Pd - OH_{ads}) + e^- \quad (2)$$

$$(Pd - OH_{ads}) + OH^- \rightarrow (Pd - O) + H_2O + e^- \quad (3)$$

For the reverse scan from +0.4 to −1.0 V, a cathodic wave appears between −0.05 and −0.55 V for Pd-blk, Pd−Ni, or Pd−Ni−P catalyst-coated electrodes as a result of reduction of the Pd−O species:[41]

$$(Pd - O) + H_2O + 2e^- \rightarrow Pd + 2OH^- \quad (4)$$

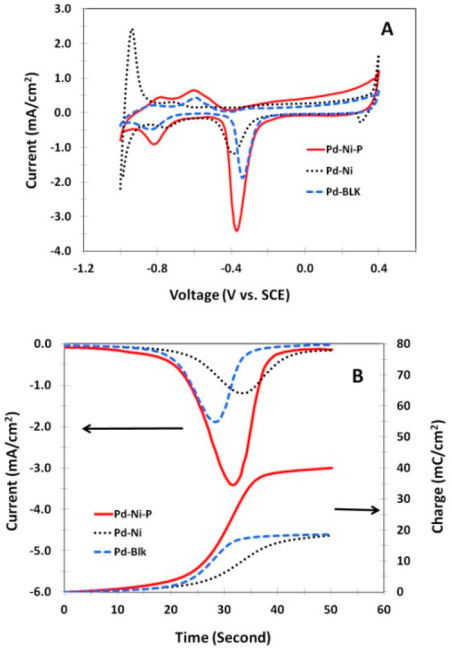

Figure 4. (A) CVs for $Pd_{0.8}Ni_{0.1}P_{0.1}$, $Pd_{0.73}Ni_{0.27}$, and Pd-black-coated GC electrodes in argon-saturated 0.1 M KOH. Note: catalyst loading is 0.2 mg/cm^2. Scan rate: 10 mV/s. (B) Integration of charges for the cathodic peaks.

However, the magnitude of cathodic current for the different catalyst-coated electrodes is different, which implies the concentration of electroactive sites on the electrodes is different. We estimated the number of Pd electroactive sites by integration of the cathodic current versus time for the cathodic scan region (see eq 5). Figure 4B shows integration of electric charges across the cathodic peak. First, we changed the *x* coordinate from voltage to time for the potential range between −0.05 and −0.55 V, which is between 0 and 50 s (the time = (voltage − 0.05)/scan rate, scan rate = 10 mV·s^{-1}), then the cumulative charges (C_{Pd}, mC cm^{-2}) in this time range was calculated.

$$C_{Pd} = \int_t^0 i \, dt \quad (5)$$

where i (mA cm^{-2}) is the current density. The calculated accumulative charges for Pd-blk-, Pd−Ni-, and Pd−Ni−P-coated electrodes are 18.6, 18.2, and 40.0 mC cm^{-2}, respectively. The coverage ($\Gamma_{pd\text{-}act}$, in mol cm^{-2}) of the electroactive Pd and the percentage of electroactive Pd (Pd_{act} %) are subsequently calculated using the following equations:

$$\Gamma_{Pd-act} = \frac{10^{-3} C_{pd}}{2F} \quad (6)$$

dx.doi.org/10.1021/cs500462z | ACS Catal. 2014, 4, 2577−2586

Table 2. Electroactive Pd and Pd % Coverage on the Electrodes Coated with the Different Synthesized Catalysts

catalyst	comp (a.u.)	C_{Pd} (mC/cm^2)	$\Gamma_{Pd\text{-}act}$ (mol/cm^2)	Pd_{act} %	Pd loading (mg/cm^2)
Pd−Ni−P	$Pd_{0.8}Ni_{0.1}P_{0.1}$	40.0	2.07×10^{-7}	12.03	0.18
Pd−Ni	$Pd_{0.7}Ni_{0.3}$	18.2	9.44×10^{-8}	6.04	0.17
Pd-blk	Pd-blk	18.6	9.63×10^{-8}	5.12	0.20

$$Pd_{act}\ \% = \frac{10^3 \Gamma_{Pd-act} \cdot M_{Pd}}{W_{Pd}} \quad (7)$$

where F is the faradic constant, M_{Pd} is the atomic mass of Pd (mg cm^{-2}), and W_{Pd} is the total net Pd loading (mg cm^{-2}) on the electrode. Table 2 lists the coverage of electroactive Pd and electroactive Pd % on the electrodes coated with the different catalysts. It is interesting that the order of electroactive Pd % is in the following order: Pd−Ni−P > Pd−Ni > Pd-blk.

3.4. Electrocatalytic Activity of the Ethanol Oxidation Reaction (EOR). The electrocatalytic activity of the catalysts was examined by repeating the experiments discussed in Figure 4A; however, 1.0 M ethanol was added into the electrolyte solution. Figure 5A shows the CVs of the Pd−Ni−P-, Pd−Ni-, and Pd-blk-coated GC electrodes in an argon-saturated 0.1 M KOH solution containing 1.0 M ethanol. The current density is based on the geometric electrode area. Forward scanning from −0.9 to +0.4 V, ethanol oxidation occurs, which forms a current wave across a wide potential range.

After reverse scanning from +0.4 to −0.2 V, no current is observed because the electrode is covered with an oxide layer formed from the forward scan.[41] Scanning to more negative potentials creates a current ramp and a subsequent "sharp peak" at approximately −0.3 V; the onset potential for the "sharp peak" varies with each electrocatalyst. The current ramp is attributed to ethanol oxidation at the freshly exposed catalyst surface on the electrode because the oxide layer is rapidly removed at more negative potentials. The electrochemical parameters of catalytic ethanol oxidation are summarized in Table S3 (see the SI). The Pd−Ni−P catalyst has the lowest onset potential (i.e., $E_{onset\text{-}fw}$ is 50 mV lower for Pd−Ni and Pd-blk catalysts), the most negative peak potential (i.e., $E_{p\text{-}fw}$ is 40 mV lower than that of Pd−Ni catalysts and 110 mV lower than that of Pd-blk catalyst), and the highest peak current ($i_{p\text{-}fw}$) for the forward scanning direction. However, the peak potentials for the reverse scan ($E_{p\text{-}rev}$) vary, which is probably due to the oxide covering. In addition, the Pd−Ni−P catalyst also possesses the highest peak current for the reverse scan ($i_{p\text{-}rev}$). The peak current density (i_p) at the Pd−Ni−P-catalyst-coated electrode is 18.75 mA cm^{-2} in 0.1 M KOH solution containing 1.0 M ethanol. Wang et al.[25] reported that ethanol oxidation current was 70 mA cm^{-2} at an electrode coated with carbon-supported Pd−Ni−P catalyst in 0.5 M NaOH containing 1.0 M ethanol. In comparison with Wang's results, we have studied the effect of KOH concentration on the catalytic current density for the ethanol oxidation reaction. When we increased the KOH concentration to 0.5 M, the current density increased to 110 mA cm^{-2} for catalytic ethanol oxidation at the Pd−Ni−P-catalyst-coated electrode, which is 1.6 times higher than that of Wang's result. The effect of the KOH concentration on the catalytic current density for ethanol oxidation will be further discussed in section 3.8. In addition, catalyst support also affects the catalytic current density because of better active sites dispersed in the support. Wang et al. used carbon-supported catalyst, but we used unsupported catalyst to exclude the interference of high-surface-area carbon to the analysis of the Pd−Ni−P structure.

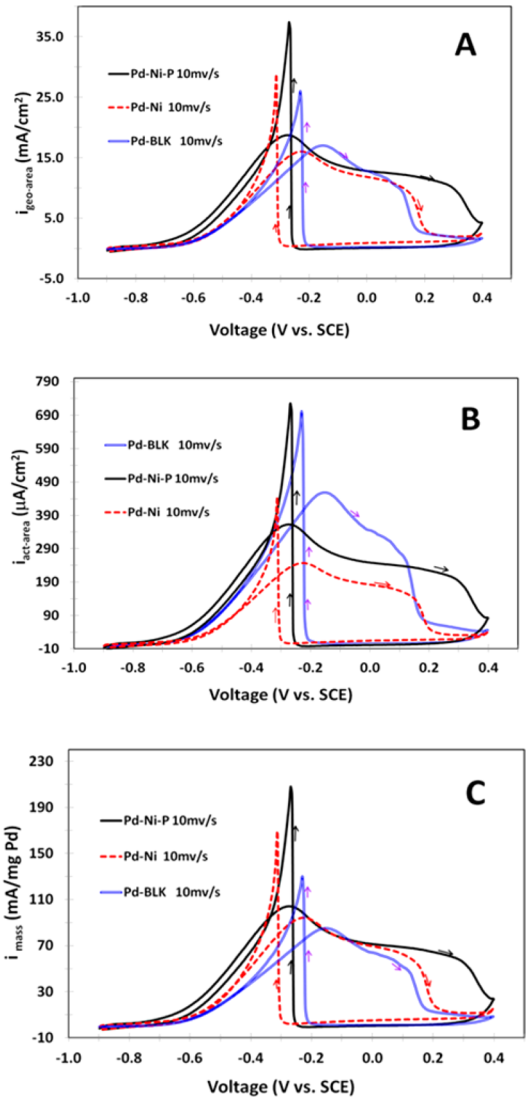

Figure 5. CVs for $Pd_{0.8}Ni_{0.1}P_{0.1}$-, $Pd_{0.7}Ni_{0.3}$-, and Pd-black-coated GC electrodes in 0.1 M KOH containing 1 M ethanol saturated with argon. Catalyst loading is 0.2 mg/cm^2. Scan rate: 10 mV/s. The current is based on geometric electrode area (A); electrochemical active surface area (B); and Pd mass loading (C).

For comparison, Figure 5A is also redrawn for the current density on the basis of the electrochemical active surface area (Figure 5B) and the mass of Pd in the catalyst coating (Figure 5C). The ratio of the electrochemical active surface area versus the geometric electrode area (or roughness factor) of the electrode was calculated by integrating the area (electric charge) of the adsorption wave for H^+/H reduction/oxidation from the corresponding cyclic voltammograms obtained in an argon-saturated solution, assuming that hydrogen is adsorbed only on Pd, not on Ni, and a 1.0 cm^2 active electrode area

dx.doi.org/10.1021/cs500462z | ACS Catal. 2014, 4, 2577−2586

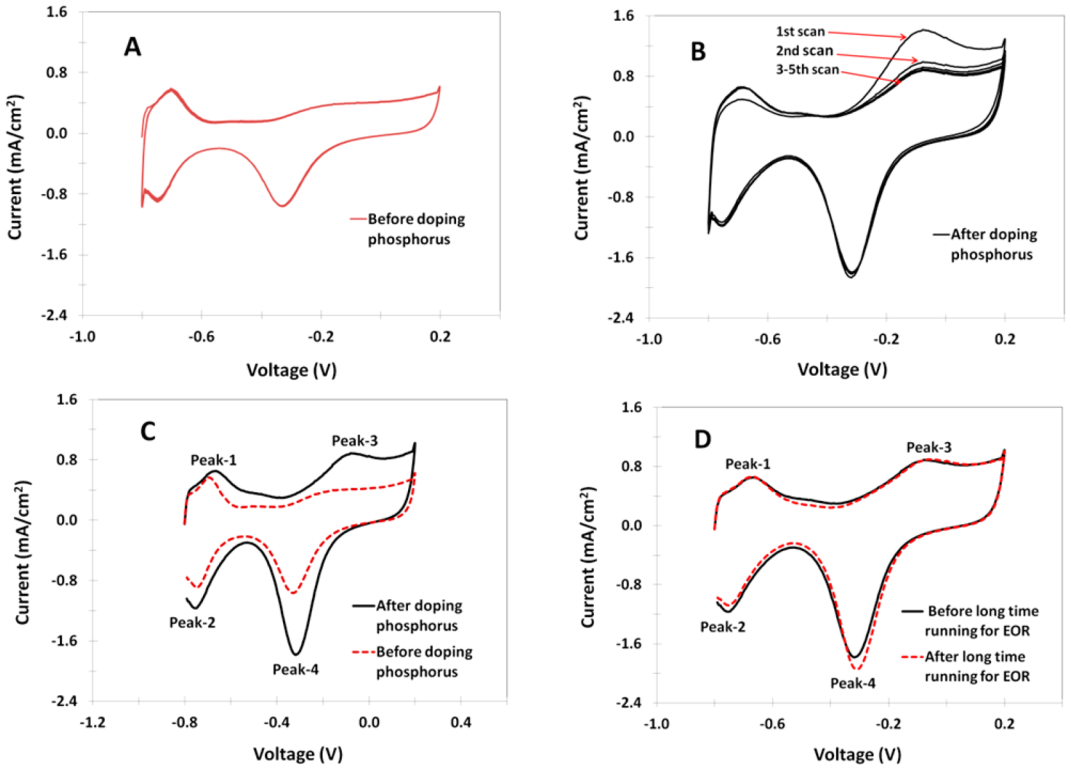

Figure 6. Cyclic voltammograms at Pd−Ni-catalyst-coated GC electrode in argon-saturated 0.1 M KOH. (A) Five consecutive scans before doping phosphorus, (B) five consecutive scans after doping phosphorus, (C) before and after doping phosphorus when the CVs were stable, and (D) CVs for the phosphorus-doped Pd−Ni GC electrode before and after long-time running for EOR.

consumed 210 uC of electric charge.[45] The roughness factors for Pd−Ni−P, Pd−Ni, and Pd-blk are 51.7, 65.0, and 37.1, respectively. Although the Pd-blk-coated electrode has the highest peak current, based on the electrochemical active surface area, it has the most positive peak potential for EOR or the highest overpotential.

3.5. Chronoamperometric Behavior of the EOR at Catalyst-Coated Electrodes. The catalytic performance of the Pd−Ni−P, Pd−Ni, and Pd-blk catalysts for the EOR was further examined by chronoamperometric tests. Figure S2-A (see the SI) shows chronoamperometric curves of the different catalyst-coated electrodes at −0.3 V in argon-saturated 0.1 M KOH containing 1 M ethanol. The highest current density is obtained for the Pd−Ni−P-coated electrode. Moreover, the current gradually reaches a plateau with increasing time for the Pd−Ni−P catalyst. Figure S2-B (see SI) shows plots of cumulative charge versus time obtained by integration of the current−time curves shown in SI Figure S2-A. The charges that were obtained for 120 min duration for Pd−Ni−P, Pd−Ni, and Pd-blk catalysts are 64.9, 53.2, and 43.9 C·cm^{-2}, respectively.

3.6. Phosphorus Dopant Stability in Electrode. We have studied the stability of phosphorus dopant in the electrode during long-time operation for catalytic ethanol oxidation in alkaline media. We used an electrochemical method to identify the existence of phosphorus in the catalyst coating. SI Figure S3-A shows cyclic voltammograms of 10 consecutive cycles at a mix of phosphorus−carbon-black-coated electrode, where the phosphorus was simply mixed with the carbon black. The peak potential (vs SCE) is at −0.14 V. It is a typical wave of phosphorus electrochemical oxidation. With an increase in the cycle number, the peak current decreases until reaching a background (compared with SI Figure S3-B, where the electrode contains carbon black only). Apparently, simply mixed phosphorus in the electrode is unstable during electrochemical oxidation.

Figures 6A and 6B show cyclic voltammograms of five consecutive scans for Pd−Ni-coated GC electrode in 0.1 M KOH before and after doping phosphorus, respectively. Before doping, the five consecutive scans are approximately repeated without current and potential changes. After doping, a new anodic wave appears with peak potential at −0.10 V. For the first a few cycles (1−4), the peak current decreases. No current decrease can be seen for the following continuously scans. It seems that some phosphorus is unstable and some phosphorus is stable in the Pd−Ni-coated electrode. It is possible that the phosphorus that is deposited on the surface of the catalyst is unstable but the phosphorus that has intercalated into the Pd−Ni crystals is stable.

Figure 6C shows cyclic voltammograms before and after doping phosphorus when a stable current was reached. It is surprising that there is a large difference in peak current for all peaks marked in Figure 6C. After the experiment shown in Figure 6C, the Pd−Ni electrode doped with phosphorus was used for catalytic ethanol oxidation in 1.0 M ethanol and 0.1 M KOH saturated with argon for a long-time operation (chronoamperometric experiment at −0.3 V vs SCE for 2 h).

Figure 6D shows cyclic voltammograms at the phosphorus-doped Pd−Ni GC electrode before and after long-time running for EOR. There are no apparent changes in peak current and peak potential for peaks 1 and 3 and only very small changes for peaks 2 and 4. Peak 3 can be assigned to the specific phosphorus peak that is stable after long-time running for catalytic ethanol oxidation in alkaline media. The stable peak 3 is relevant to the intercalated phosphorus in the Pd−Ni crystal

dx.doi.org/10.1021/cs500462z | ACS Catal. 2014, 4, 2577−2586

structure. The height of the peak current of peak 3 is an indication of the amount of intercalated phosphorus. Therefore, we believe a large part of the phosphorus is intercalated into the Pd−Ni structure in the doping process in the presence of a phosphorus source, forming a new Pd−Ni−P structure. The intercalated phosphorus in the Pd−Ni−P catalyst is very stable after a long-time catalytic reaction for EOR in an alkaline electrolyte. Some phosphorus is only simply deposited on the surface of the Pd−Ni catalyst, which is not stable in alkaline media and is stripped off during the electrochemical oxidation process.

3.7. Steady-State Voltammetry and Tafel Slope Analysis. Voltammetric scans with very slow scan rate (2 mV/s) were carried out in addition to the chronoamperometric and CVs previously discussed. The slow scan rate evaluates the electrocatalysts approximating the steady state.

Figure 7A shows linear potential scans at a very slow scan rate (2 mV/s) for Pd−Ni−P-, Pd−Ni-, and Pd-blk-coated GC

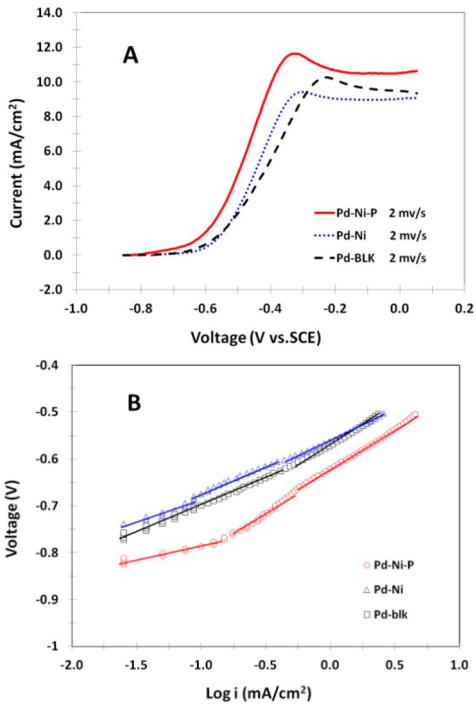

Figure 7. (A) Linear potential scan at very slow scan rate (2 mv/s) of $Pd_{0.8}Ni_{0.1}P_{0.1}$, $Pd_{0.7}Ni_{0.3}$, and Pd-blk-coated GC electrodes in argon-saturated 0.1 M KOH containing 1 M ethanol. (B) Tafel plots derived from the polarization curves in part A.

electrodes in argon-saturated 0.1 M KOH containing 1 M ethanol. The current reaches a plateau for each of the potential scans when the voltage is higher than −0.2 V. The low current portion of the polarization curves (i.e., potentials less than −0.5 V) was used for Tafel plots. Figure 7B shows Tafel plots obtained from Figure 7A. Each of the Tafel plots can be divided into two or three straight lines for the low, middle, and high polarization regions. The values of the Tafel slopes are summarized in Table S4 (see Supporting Information). For the low polarization region, the Tafel slopes for Pd−Ni−P-, Pd−Ni-, and Pd-blk-coated electrodes are 60, 92, and 117 mV·dec^{-1}, respectively. The smallest Tafel slope is seen for the Pd−Ni−P-coated electrode within the low polarization region. In the middle and high polarization ranges, the electrode process is complicated by the formation of oxides and the presence of intermediate products on the electrode surface. In contrast to the low polarization region, the Pd−Ni catalyst exhibits the smallest Tafel slope in the middle and high polarization regions. For comparison, in low overpotential range, the Pd−Ni−P is more active (with lower Tafel slope) than Pd−Ni, but in high overpotential range, the activity of the Pd−Ni catalyst is much improved (with lower Tafel slope). However, the overall catalyst performance is determined by multiple factors, including Tafel slope, onset potential, peak potential and peak current for catalytic ethanol oxidation. Because the Pd−Ni−P electrode also has more negative onset potential, more negative peak potential, and higher peak current for EOR, the Pd−Ni−P electrode has better catalytic activity than the Pd−Ni electrode.

3.8. EOR Mechanistic Discussion at the Pd−Ni−P Electrocatalyst. The electrocatalytic oxidation of ethanol is complex and may result in various final products, including an undesirable acetaldehyde (CH_3CHO) product, an undesirable acetic acid (CH_3COOH) product and/or a desirable carbon dioxide (CO_2) product. In alkaline solution, the possible ethanol electroreactions are

$$CH_3CH_2OH + 2OH^- \rightarrow CH_3CHO + 2H_2O + 2e^- \quad (8)$$

$$CH_3CH_2OH + 5OH^- \rightarrow CH_3COO^- + 4H_2O + 4e^- \quad (9)$$

$$CH_3CH_2OH + 16OH^- \rightarrow 2CO_3^{2-} + 11H_2O + 12e^- \quad (10)$$

Liang and Zhao et al.[41] studied the various products of ethanol electrooxidation. Their experiments confirmed that acetaldehyde is oxidized at the Pd-black-coated electrode in alkaline media, resulting in a high catalytic current; however, no catalytic current for acetic acid electrooxidation was observed at the same Pd-coated electrode. Here, we use the same method to determine the electron number of the catalytic ethanol oxidation at Pd−Ni−P-catalyst-coated electrode. Figure S4 (see Supporting Information) shows cyclic voltammograms of Pd−Ni−P-catalyst-coated GC electrodes in 0.1 M KOH in the presence and absence of 1 M potassium acetate (KAc). Unfortunately, there is no anodic current increase after adding acetate in the electrolyte solution, and the cyclic voltammograms show no apparent difference for the presence and absence of 1.0 M potassium acetate. This experiment leads us to believe that the Pd−Ni−P electrode catalyzes the ethanol oxidation via a 4-electron process to acetate, which means there is no C−C bond breakage. In addition, eq 9 may be split into the following steps,[41]

$$Pd + CH_3CH_2OH \leftrightarrow (Pd{-}CH_3CH_2OH_{ads}) \quad (11)$$

$$(Pd{-}CH_3CH_2OH_{ads}) + 3OH^- \rightarrow (Pd{-}CH_3CO_{ads}) + 3H_2O + 3e^- \quad (12)$$

$$Pd + OH^- \rightarrow (Pd{-}OH_{ads}) + e^- \quad (2b)$$

$$(Pd{-}CH_3CO_{ads}) + (Pd{-}OH_{ads}) \rightarrow (Pd{-}CH_3COOH) + Pd \quad (13)$$

$$(Pd{-}CH_3COOH) + OH^- \rightarrow Pd + CH_3COO^- + H_2O \quad (14)$$

dx.doi.org/10.1021/cs500462z | ACS Catal. 2014, 4, 2577−2586

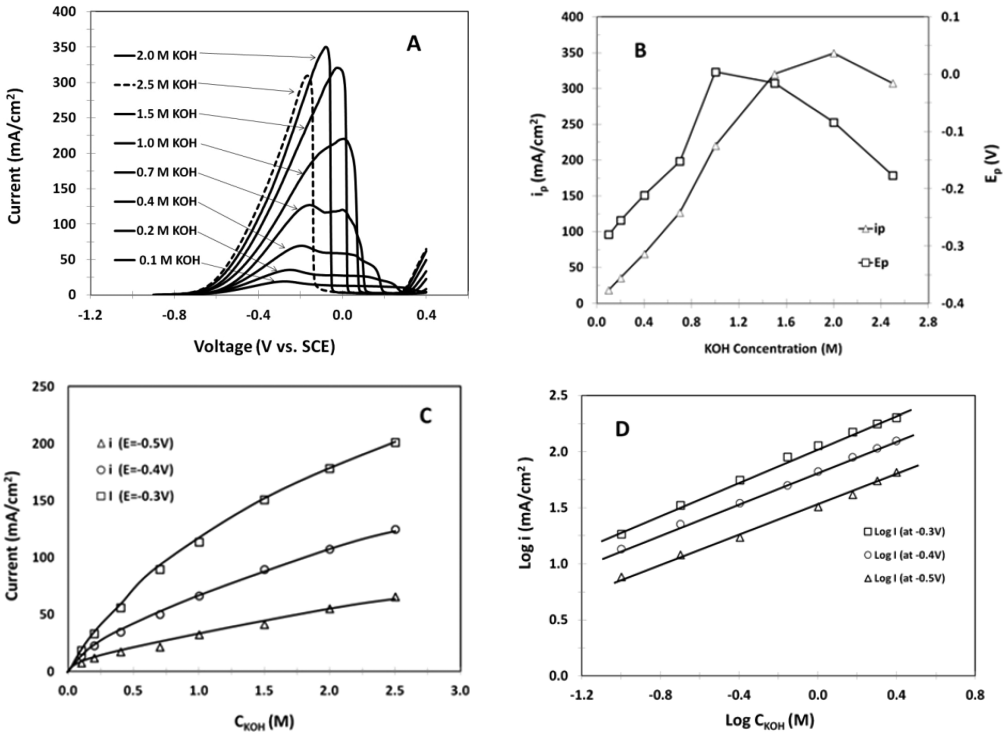

Figure 8. (A) Linear potential scan (−0.9 V to +0.4 V) of $Pd_{0.8}Ni_{0.1}P_{0.1}$-coated GC electrodes in different concentrations of KOH solution containing 1 M ethanol, (B) plots of i_p and E_p versus KOH concentration, (C) plots of current at different potentials versus KOH concentration, and (D) plots of log i versus log C_{KOH}. Catalyst loading, 0.2 mg/cm^2. Scan rate, 10 mV/s.

The mechanisms of ethanol electrooxidation at Pd or Pd-based alloy catalyst have been discussed in the literature, and it is generally accepted that the stripping of the adsorbed ethoxi species and the acetate-releasing step from catalytic sites is the rate-determining step.[29,41,42] The catalytic kinetic process of EOR at the Pd−Ni−P-catalyst-coated electrode is further analyzed and presented in the following section.

3.9. EOR Kinetic Processes at the Pd−Ni−P Electrocatalyst. The electrocatalytic process of the EOR at the Pd−Ni−P-catalyst-coated electrode is further analyzed by measuring the effect of KOH concentration (C_{KOH}) and ethanol concentration (C_{EtOH}) on the catalytic current. At steady-state conditions, the catalytic current is expressed as[41,43,44]

$$i = nFAK_f C_{EtOH}{}^{b} C_{KOH}{}^{a} \quad (15)$$

Here, i is current density (mA·cm^{-2}), n is the electron number of EOR, F is the faradic constant and K_f is reaction rate constant that is potential-dependent. C_{KOH} and C_{EtOH} are the concentrations of KOH and ethanol in electrolyte solution, and the superscripts "a" and "b" are reaction orders with respect to KOH and ethanol concentrations, respectively. Equation 15 may be rewritten as

$$\log(i) = \log(nFK_f C_{EtOH}{}^{b}) + a\cdot\log(C_{KOH}) \quad (16)$$

When the electrode potential and the ethanol concentration (1 M) are held constant, we have

$$\log(i) = A + a\cdot\log(C_{KOH}) \quad (17)$$

$$A = \log(nFK_f C_{EtOH}{}^{b}) \quad (18)$$

where A is a new constant. The reaction order ("a" value) with respect to KOH concentration is obtained from the slope by plotting log i versus log C_{KOH}. The reaction rate constant K_f is then obtained from the intercept (A value) once we know the reaction order (b value) with respect to the ethanol concentration.

Figure 8A shows a linear potential scan of Pd−Ni−P-coated GC electrodes in different concentrations of KOH solution containing 1.0 M ethanol. The catalytic current of ethanol oxidation is very sensitive to the KOH concentration. The peak current (i_p) is increased from 19 to 350 mA/cm^2 when the KOH concentration is changed from 0.1 to 2.0 M. Figure 8B shows plots of peak current and peak potential (E_p) versus KOH concentration. If the KOH concentration is more than 2.0 M, the peak current begins to drop because a thicker oxide layer is formed, as shown in eq 3. The peak potential increases with increasing KOH concentration until reaching 1.0 M, and then it decreases, which is also attributed to the oxide layer growth at the electrode surface. Figure 8C shows plots of the current at different potentials versus the KOH concentration. These plots are not straight lines and curve downward with increasing KOH concentration. The downward curve indicates that OH^- ions are kinetically involved in the ethanol electrooxidation reaction. Figure 8D shows plots of log i versus log C_{KOH}, in which the slopes are used to calculate reaction orders. The reaction orders at different electrode potentials are listed in Table S5 (see Supporting Information). From the intercept A, we calculated the reaction rate constant K_f with a known b value (See Table 3).

When the electrode potential and the KOH concentration (1.0 M) are not changed, we have

$$\log(i) = \log(nFK_f C_{KOH}{}^{a}) + b\cdot\log(C_{EtOH}) \quad (19)$$

$$\log(i) = B + b\cdot\log(C_{EtOH}) \quad (20)$$

$$B = \log(nFK_f C_{KOH}{}^{a}) \quad (21)$$

dx.doi.org/10.1021/cs500462z | ACS Catal. 2014, 4, 2577−2586

Table 3. Rate Constants, K_f, for the electrocatalytic ethanol oxidation Reaction at the Pd−Ni−P Catalyst in Alkaline Electrolyte

potential (V vs SCE)	K_f (cm s^{-1} M^{-1}) obtained from Figure 8D and eq 17	K_f (cm s^{-1} M^{-1}) obtained from SI Figure S5 and eq 20
−0.3	2.8×10^{-4}	2.7×10^{-4}
−0.4	1.7×10^{-4}	1.6×10^{-4}
−0.5	0.87×10^{-4}	0.78×10^{-4}

where we use the slope to calculate the reaction orders at different electrode potentials and the intercept B to calculate the reaction rate constant K_f, (see Figure S5 in Supporting Information). The reaction orders at different potentials are calculated with eq 20 and are listed in Table S5 (see Supporting Information). The reaction order with respect to ethanol concentration increases slightly with increasing electrode potential, yielding an average reaction order of 0.52. The reaction order agrees well with that for methanol electrooxidation on a PtRu-coated electrode in 0.5 M H_2SO_4 solution, which was previously reported by Chu and Gilman et al.[43] The reaction order of ethanol electrooxidation is slightly lower than that reported by Pandey et al.,[44] who reported a reaction order of 0.57 for ethanol electrooxidation at Au-PANI-coated electrode in 0.5 M NaOH. The reaction rate constants, K_f, at different potentials are calculated from the intercepts with eq 20, and are listed in Table 3. As expected, for a given electrode potential, the value of K_f obtained with SI Figure S5-D is the same as that obtained with Figure 8D, with only small deviations between experiments.

CONCLUSIONS

A class of electrocatalysts containing metal/nonmetal elements has been proposed. The Pd−Ni−P compound contains Ni and P atoms that modify the crystal structure, and charge transfer to the nearby Pd atoms proved to be relevant for the EOR catalytic activity in alkaline media. For comparison, unsupported Pd−Ni−P and Pd−Ni catalysts were synthesized with $Pd_{0.8}Ni_{0.1}P_{0.1}$ and $Pd_{0.7}Ni_{0.3}$ (a.u.) compositions, respectively. The Pd−Ni−P catalyst structure was more amorphous with smaller particle sizes than the Pd−Ni and Pd-blk samples, as determined by XRD, TEM, and BET surface area analyses. After alloying Pd with Ni, the XRD results indicate that the 2θ value at peak position shifts to larger values, whereas the d-spacing becomes decreased, which implies that the Pd lattice structure shrinks after alloying with Ni. However, after doping Pd−Ni with P, the 2θ peak position shifts to smaller values, and the d-spacing increases, which indicates that the Pd−Ni lattice structure expands after doping with P. The Pd−Ni−P catalyst was found to have more active electrocatalytic sites than the Pd−Ni and Pd-blk catalysts in alkaline media. For the EOR in 0.1 M KOH, the Pd−Ni−P catalyst was proved to have the more negative onset potential, the most negative peak potential, and the highest catalytic current. In addition, there was a 110 mV reduction of overpotential in comparison with the Pd-blk catalyst for catalytic ethanol oxidation in alkaline media. For the Pd−Ni−P, a Tafel slope of ∼60 mV/dec was observed for the EOR in low polarization potential range, whereas larger Tafel slopes were observed for the Pd−Ni (92 mv/dec) and the Pd-blk (117 mv/dec) samples. The reaction orders of EOR at the Pd−Ni−P-coated electrode with respect to KOH and ethanol concentrations are 0.7 and 0.5, respectively. The electrooxidation of ethanol at the Pd−Ni−P catalyst reveals a four-electron oxidation to acetate with a reaction rate constant of 2.8×10^{-4} cm S^{-1} M^{-1} at −0.3 V vs SCE in KOH media.

ASSOCIATED CONTENT

Supporting Information

EDS, BET surface area, XRD, and electrochemical data of EOR. This material is available free of charge via the Internet at http://pubs.acs.org.

AUTHOR INFORMATION

Corresponding Author

*Phone: 301-394-0295. E-mail: Rongzhong.jiang.civ@mail.mil.

Notes

The authors declare no competing financial interest.

ACKNOWLEDGMENTS

The authors would like to thank Dr. Panju Shang at University of Maryland for assisting TEM analysis. Thanks to Dr. Cynthia Lundgren for helpful discussions. Finally, thanks to the U.S. Department of the Army and U.S. Army Materiel Command for supporting this work.

REFERENCES

(1) Marcinkoski, J.; James, B. D.; Kalinoski, J. A.; Podolski, W.; Benjamin, T.; Kopasz, J. *J. Power Sources* **2011**, *196*, 5282−5292.
(2) Wang, D.; Xin, H. L.; Yu, Y. C.; Wang, H. S.; Rus, E.; Muller, D. A.; Abruna, H. D. *J. Am. Chem. Soc.* **2010**, *132*, 17664−17666.
(3) Oezaslan, M.; Hasché, F.; Strasser, P. *J. Phys. Chem. Lett.* **2013**, *4*, 3273−3291.
(4) Wu, J. B.; Yang, H. *Acc. Chem. Res.* **2013**, *46*, 1848−1857.
(5) Zhang, H. X.; Wang, C.; Wang, J. Y.; Zhai, J. J.; Cai, W. B. *J. Phys. Chem. C* **2010**, *114*, 6446−6451.
(6) Lima, F. H. B.; de Castro, J. F.R.; L. Santos, G. R. A.; Ticianelli, E. A. *J. Power Sources* **2009**, *190*, 293−300.
(7) Rong, C.; Jiang, R. Z.; Sarney, W.; Chu, D. *Electrochim. Acta* **2010**, *55*, 6872−6878.
(8) Karim, N. A.; Kamarudin, S. K. *Appl. Energy* **2013**, *103*, 212−220.
(9) Serov, A.; Kwak, C. *Appl. Catal., B* **2009**, *90*, 313−320.
(10) Garsuch, A.; d'Eon, R.; Dahn, T.; Klepel, O.; Garsuch, R.; Dahn, J. R. *J. Electrochem. Soc.* **2008**, *155*, B236−B243.
(11) Jiang, R. Z.; Chu, D. *J. Power Sources* **2014**, *245*, 352−361.
(12) Bezerra, C. W. B.; Zhang, L.; Lee, K. C.; Liu, H. S.; A. Marques, L. B.; Marques, E. P.; Wang, H. J.; Zhang, J. J. *Electrochim. Acta* **2008**, *53*, 4937−4951.
(13) Merle, G.; Wessling, M.; Nijmeijer, K. *J. Membr. Sci.* **2011**, *377*, 1−35.
(14) Gao, Y. W.; Wang, G.; Wu, B.; Deng, C.; Gao, Y. *J. Appl. Electrochem.* **2011**, *41*, 1−6.
(15) Qi, Z.; Geng, H. R.; Wang, X. G.; Zhao, C. C.; Ji, H.; Zhang, C.; Xu, J. L.; Zhang, Z. H. *J. Power Sources* **2011**, *196*, 5823−5828.
(16) Jin, C. C.; Sun, X. J.; Chen, Z. D.; Dong, R. L. *Mater. Chem. Phys.* **2012**, *135*, 433−437.
(17) Li, R. S.; Mao, H.; Zhang, J. J.; Huang, H.; Yu, A. S. *J. Power Sources* **2013**, *241*, 660−667.
(18) Fu, G. T.; Wu, K.; Lin, J.; Tang, Y. W.; Chen, Y.; Zhou, Y. M.; Lu, T. H. *J. Phys. Chem. C* **2013**, *117*, 9826−9834.
(19) Dutta, A.; Datta, J. *J. Phys. Chem. C* **2012**, *116*, 25677−25688.
(20) Shen, S. Y.; Zhao, T. S.; Xu, J. B.; Li, Y. S. *J. Power Sources* **2010**, *195*, 1001−1006.
(21) Zheng, H. T.; Li, Y. L.; Chen, S. X.; Shen, P. K. *J. Power Sources* **2006**, *163*, 371−375.
(22) Yang, G. X.; Chen, Y.; Zhou, Y. M.; Tang, Y. W.; Lu, T. H. *Electrochem. Commun.* **2010**, *12*, 492−495.
(23) Zhang, L. L.; Tang, Y. W.; Bao, J. C.; Lua, T. H.; Li, C. *J. Power Sources* **2006**, *162*, 177−179.

(24) Wang, J. Y.; Kang, Y. Y.; Yang, H.; Cai, W. B. *J. Phys. Chem. C* **2009**, *113*, 8366−8372.
(25) Wang, Y.; Shi, F. F.; Yang, Y. Y.; Cai, W. B. *J. Power Sources* **2013**, *243*, 369−373.
(26) Ding, L. X.; Wang, A. L.; Li, G. R.; Liu, Z. Q.; Zhao, W. X.; Su, C. Y.; Tong, Y. X. *J. Am. Chem. Soc.* **2012**, *134*, 5730−5733.
(27) Xue, X. Z.; Ge, J. J.; Tian, T.; Liu, C. P.; Xing, W.; Lu, T. H. *J. Power Sources* **2007**, *172*, 560−569.
(28) Sekol, R. C.; Carmo, M.; Kumar, G.; Gittleson, F.; Doubek, G.; Sun, K.; Schroers, J.; Taylor, A. D. *Int. J. Hydrogen Energy* **2013**, *38*, 11248−11255.
(29) Yu, E. H.; Krewer, U.; Scott, K. *Energies* **2010**, *3*, 1499−1528.
(30) Liu, J. P.; Zhou, H. H.; Wang, Q. Q.; Zeng, F. Y.; Kuang, Y. F. *J. Mater. Sci.* **2012**, *47*, 2188−2194.
(31) Oliveira, M. C.; Rego, R.; Fernandes, L. S.; Tavares, P. B. *J. Power Sources* **2011**, *196*, 6092−6098.
(32) Verma, A.; Basu, S. *J. Power Sources* **2007**, *174*, 180−185.
(33) Antolini, E.; Gonzalez, E. R. *J. Power Sources* **2010**, *195*, 3431−3450.
(34) Xu, C. W.; Wang, H.; Shen, P. K.; Jiang, S. P. *Adv. Mater.* **2007**, *19*, 4256−4259.
(35) Bagchi, J.; Bhattacharya, S. K. *J. Power Sources* **2007**, *163*, 661−670.
(36) Bianchini, C.; Bambagioni, V.; Filippi, J.; Marchionni, A.; Vizza, F.; Bert, P.; Tampucci, A. *Electrochem. Commun.* **2009**, *11*, 1077−1080.
(37) Hu, F. P.; Chen, W. X. *Electrochem. Commun.* **2011**, *13*, 955−958.
(38) He, Q. G.; Shyam, B.; Macounova, K.; Krtil, P.; Ramaker, D.; Mukerjee, S. *J. Am. Chem. Soc.* **2012**, *134*, 8655−8661.
(39) Wang, J. Y.; Peng, B.; Xie, H. N.; Cai, W. B. *Electrochim. Acta* **2009**, *54*, 1834−184.
(40) Hines, W. A.; Glover, K.; Clark, W. G.; Kabacoff, L. T.; Modzelewski, C. U.; Hasegawa, R.; Duwez, P. *Phys. Rev. B* **1980**, *21*, 3771−3780.
(41) Liang, Z. X.; Zhao, T. S.; Xu, J. B.; Zhu, L. D. *Electrochim. Acta* **2009**, *54*, 2203−2208.
(42) Mahapatra, S. S.; Dutta, A.; Datta. *J. Electrochim. Acta* **2010**, *55*, 9097−9104.
(43) Chu, D.; Gilman, S. *J. Electrochem. Soc.* **1996**, *143*, 1685−1690.
(44) Pandey, R. K.; Lakshminarayanan, V. *Appl. Catal., B* **2012**, *125*, 271−281.
(45) Koffi, R. C.; Coutanceau, C.; Garnier, E.; Leger, L. M.; Lamy, C. *Electrochim. Acta* **2005**, *50*, 4117−4127.